Available online at www.sciencedirect.com
SCIENCE DIRECT
NDT&E International 39 (2006) 414–424
NDT&E international
www.elsevier.com/locate/ndteint

Calculation and simulation of impedance diagrams of planar rectangular spiral coils for eddy current testing

Javier O. Fava *, Marta C. Ruch

Non-Destructive and Structural Testing Department, Centro Atómico Constituyentes, Comisión Nacional de Energía Atómica, Av. General Paz 1499, 1650 San Martín, Buenos Aires, Argentina

Received 26 August 2005; received in revised form 17 November 2005; accepted 4 December 2005
Available online 7 February 2006

Abstract

The knowledge of analytical expressions for the electromagnetic (EM) fields produced by the coils used in eddy current testing is an important point in the development and application of these devices. In the present work, the second order vector potential formulation is used for the calculation of the fields produced by planar rectangular spiral coils of arbitrary number of turns and finite rectangular cross-section placed on a conducting half-space. Impedance plane diagrams are calculated for different frequencies, lift-off and half-space conductivity. Tests for conductivity assessment are also simulated. The theoretical results are compared with experimental measurements.

Keywords: Eddy current testing; Impedance diagram; Rectangular planar coils; Resistivity assessment

1. Introduction

The use of planar coils for defect detection and materials characterization has been reported by many authors [1–6]. Our group has been working for some years on the design, characterization and use of planar rectangular coils [7,8]. For the design and construction of the coils described used in the cited papers simple models have been used, through which only the electrical parameters of the coils could be calculated: L_0, R and C. The experience acquired in those early works gave us an insight of the advantages of this type of coils: elimination of end effect in the inspection of edge cracks, good performance in the conductivity measurement at high frequencies, high sensitivity to crazing and other shallow imperfections, and the fact that any number of identical planar coils can be made from a single photographic negative. It also presented us with the challenge to extend our understanding of the scope and limitations of this type of coils. To achieve this, a knowledge of the expressions of the EM fields they produce is fundamental.

In this work, the calculations of the EM fields and the expressions for inductance and impedance are first presented, following the same steps as other authors [9,10]. Thus, the expressions for field calculations are derived in the second order vector potential formulation. The formulae are then applied to the calculation of coil inductance in air, L_0, and to modeling of the impedance plane of the coils under study.

In this way, a generalization of the results by Theodoulidis et al. [9] was achieved. In particular in the present paper results from three planar coils are presented: two of them consist of two planar windings of 6 and 10 turns, respectively, placed on the opposite faces of an isolating substrate, the third one consists of two planar 7-turn windings, both of them placed on the same face of the isolating substrate. These results may be extended to flat rectangular coils with finite rectangular cross-section and any number of turns.

2. Problem definition

A sketch of the problem to be solved is shown in Fig. 1: a source $\mathbf{J}$ of alternate current above an infinite isotropic, homogeneous, conducting, non-ferromagnetic half-space of electrical conductivity σ and magnetic permeability μ. Here, $\mu = \mu_0\mu_r$ with μ_0 the permeability of free space and μ_r the relative permeability.

The EM fields produced by the source in all the space are to be calculated. For this task, the second order potential vector formulation [11] under the quasi-static approximation was used.

* Corresponding author. Tel.: +54 11 6772 7233; fax: +54 11 6772 7355.
E-mail address: fava@cnea.gov.ar (J.O. Fava).

0963-8695/$ - see front matter © 2005 Elsevier Ltd. All rights reserved.
doi:10.1016/j.ndteint.2005.12.002

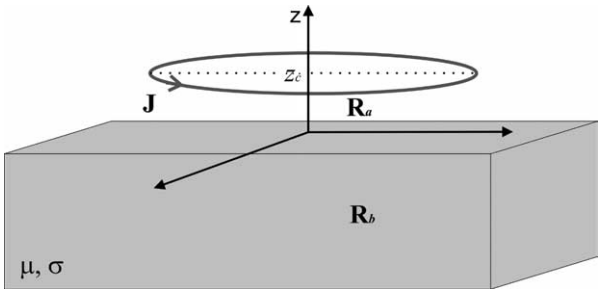

Fig. 1. Current distribution in an infinite conducting half-space and the regions of interest. $z=0$ corresponds to the interface separating the media.

The source is excited with a sinusoidal current density of frequency f: $\mathbf{J}(\mathbf{x}, t)=\mathbf{J}_0(\mathbf{x})e^{j\omega t}$ with $\omega=2\pi f$. In the Coulomb gauge ($\nabla\cdot\mathbf{A}=0$) [12], the existence of a second order vector potential $\mathbf{W}$ can be assumed, such that $\mathbf{A}=\nabla\times\mathbf{W}$. Following [11] we write $\mathbf{W}$ as

$$\mathbf{W}_{a,b}=\hat{\mathbf{z}}W_{1,a,b}+\hat{\mathbf{z}}\times\nabla\cdot W_{2,a,b} \tag{1}$$

with $\hat{\mathbf{z}}$ the unit vector in the z-axis direction and W_1 and W_2 the two independent scalar potentials on which $\mathbf{W}$ depends. Because we are working in the Coulomb gauge and in a region free of electric charge sources ($\rho(\mathbf{x}, t)=0$), the electric potential is zero ($\phi(\mathbf{x}, t)=0$) and the vector potential $\mathbf{A}$ satisfies Eq. (2) in each of the regions of space of interest to the present problem:

$$\nabla^2\mathbf{A}_{a,b}+\mu_{a,b}\varepsilon_{a,b}\omega^2\mathbf{A}_{a,b}=-\mu_{a,b}\mathbf{J}_{a,b}, \tag{2}$$

The sub indices a and b indicate the a and b regions into which the problem has been divided for its study, where $\mathbf{D}_{a,b}=\varepsilon_0\mathbf{E}_{a,b}$ because $\varepsilon_a=\varepsilon_b=\varepsilon_0$; $\mathbf{B}_a=\mu_0\mathbf{H}_a$, $\mathbf{B}_b=\mu\mathbf{H}_b$, $\mathbf{J}_a=0$ and $\mathbf{J}_b=\sigma\mathbf{E}_b$, and the fields are given by $\mathbf{E}_{a,b}=-\partial\mathbf{A}_{a,b}/\partial t$ and $\mathbf{B}_{a,b}=\nabla\times\mathbf{A}_{a,b}$. With these expressions, Eq. (2) can be written as follows in terms of the vector potential:

$$\nabla^2\mathbf{A}_{a,b}-j\mu_{a,b}\sigma_{a,b}\omega\mathbf{A}_{a,b}+\mu_{a,b}\varepsilon_{a,b}\omega^2\mathbf{A}_{a,b}=0. \tag{3}$$

For metals and the test frequencies ordinarily used in electromagnetic nondestructive testing (under 10 MHz), the value of $\mu\sigma\omega$ greatly exceeds that of $\mu\varepsilon\omega^2$, so that the third term in (3) can be disregarded [13]. This is known as the quasi-static approximation. The equations for $\mathbf{A}$ can thus be written

$$\nabla^2\mathbf{A}_a=0 \tag{4}$$

$$\nabla^2\mathbf{A}_b-\gamma^2\mathbf{A}_b=0, \tag{5}$$

with $\gamma^2=j\omega\mu\sigma$.

In the region, R_a Laplace equation (4) is also true for $\mathbf{W}_a$, therefore $\nabla^2W_{1a}=0$ and $\nabla^2W_{2a}=0$. $\mathbf{A}_a$ consequently takes the form

$$\mathbf{A}_a=\nabla\times\hat{\mathbf{z}}W_{1a}-(\hat{\mathbf{z}}\cdot\nabla)\nabla W_{2a}, \tag{6}$$

and the corresponding magnetic flux density is

$$\mathbf{B}_a=\nabla\left(\frac{\partial W_{1a}}{\partial z}\right) \tag{7}$$

In the region, R_a the vector potential is the sum of the primary potential $\mathbf{A}_{ap}$ produced by the excitation current in the coil and the secondary potential $\mathbf{A}_{as}$ originated in the eddy currents within the conductive halfspace: $\mathbf{A}_a=\mathbf{A}_{ap}+\mathbf{A}_{as}$. W_{1a} will thus consist of the same contributions $W_{1a}=W_{1ap}+W_{1as}$, each of them satisfying Laplace equation:

$$\nabla^2W_{1ap}=0 \tag{8}$$

and

$$\nabla^2W_{1as}=0. \tag{9}$$

For the calculation of the vector potential in the region R_b, there is in principle the equation derived from (1). As it is known [14,15], from the continuity of the tangential component of the magnetic field intensity and of the normal component of the magnetic flux density, the boundary conditions for the scalar potentials at the interface between both media ($z=0$) can be determined.

The conditions which W_{2b} must satisfy are: $\partial W_{2b}/\partial z=0$ and $W_{2b}=0$, and because there are no sources in the conductor, W_{2b} must be zero in the conductor. Thus, the expression for the vector potential is

$$\mathbf{A}_b=\nabla\times\hat{\mathbf{z}}W_{1b}, \tag{10}$$

and substituting this expression in (5), an analogous equation for W_{1b} is obtained

$$\nabla^2W_{1b}-\gamma^2W_{1b}=0. \tag{11}$$

The solution to this problem is fully determined once Eqs. (8), (9) and (11) are solved. Therefore, it is only necessary to know one scalar potential W_1, all over the space. These equations have general solutions, which can be written in terms of double Fourier transforms. W_{1ap} is obtained from the calculation of $\mathbf{A}_{1ap}$ for a known current distribution, as discussed in Section 3.

The solutions of Eqs. (9) and (11) in terms of the Fourier transforms of W_{1as} and W_{1b}, [16], which we denote $X_{1as}(\alpha,\beta,??z)$ and $X_{1b}(\alpha,\beta,z)$, respectively, are

$$X_{1as}(\alpha,\beta,z)=K_{1as}(\alpha,\beta)e^{-kz} \text{ and}$$
$$X_{1b}(\alpha,\beta,z)=K_{1b}(\alpha,\beta)e^{\lambda z}, \text{ with } k^2=\alpha^2+\beta^2 \text{ and}$$
$$\lambda^2=k^2+\gamma^2.$$

If a solution for W_{1ap} is known

$$W_{1ap}=F^{-1}[X_{1ap}]=\int_{-\infty}^{+\infty}\int_{-\infty}^{+\infty}K_{1ap}(\alpha,\beta)e^{kz}e^{j(\alpha x+\beta y)}d\alpha\,d\beta, \tag{12}$$

with $F^{-1}[X_{1ap}]$ the inverse Fourier transform of X_{1ap}. The expressions for the K_{1as} and K_{1b} coefficients are determined applying the boundary conditions for $\mathbf{B}$ and $\mathbf{H}$ at $z=0$ in terms of the scalar potentials. Thus, the scalar potentials are

$$W_{1as}=\int_{-\infty}^{+\infty}\int_{-\infty}^{+\infty}K_{1ap}(\alpha,\beta)\frac{\mu_r k-\gamma}{\mu_r k+\gamma}e^{-kz}e^{j(\alpha x+\beta y)}d\alpha\,d\beta, \tag{13}$$

$$W_{1b} = \int_{-\infty}^{+\infty}\int_{-\infty}^{+\infty} K_{1ap}(\alpha,\beta)\frac{2\mu_r k}{\mu_r k+\gamma} e^{\lambda z} e^{j(\alpha x+\beta y)} d\alpha\, d\beta. \quad (14)$$

3. Rectangular coils

3.1. Single wire rectangular current loop

As above indicated, first W_{1ap} for the current distribution under study must be determined in order to be able to calculate the expressions for the other scalar potentials using (13) and (14). We start with the expression for the magnetic flux density of a current loop calculated using the corresponding vector potential [17]

$$\mathbf{B}_a = \nabla\times\mathbf{A}_a = \nabla\times\left[\frac{\mu_0}{4\pi}\int_{V_S}\frac{\mathbf{J}(\mathbf{r}_s)}{r}dV_S\right]$$

$$= \nabla\times\left[\frac{\mu_0 I}{4\pi}\oint_C \frac{d\mathbf{l}}{r}\frac{\mathbf{dl}}{\mathbf{r}}\right] \quad (15)$$

with $r=\sqrt{(x-x_s)^2+(y-y_s)^2+(z-z_s)^2}$, where $\mathbf{r}_s=(x_s, y_s, z_s)$ is a current source point and $r=(x, y, z)$ is a field point. After using Stokes' theorem, rearranging, comparing our result with (7) and solving for W_{1ap}, we get

$$W_{1ap} = -\frac{\mu_0 I}{4\pi}\int_S \hat{\mathbf{z}}\nabla_s\left(\int\frac{dz}{r}\right)da. \quad (16)$$

For the calculation of W_{1ap}, let the current source circulate along a conducting wire in the shape of a rectangular loop, Fig. 2. Due to the design of the coils under study in the present work (Section 3.2), for the calculations two loops must be considered, one centered at $(0, 0, z_c)$ and the other at (x', y', z_c).

When expression (16) is applied to these distributions, the desired results for W_{1ap} are obtained. For the distribution in Fig. 2 (loop centred at $(0, 0, z_c)$) we use the expression presented in [9]:

$$W_{1ap} = \frac{\mu_0 I}{2\pi^2}\int_{-\infty}^{+\infty}\int_{-\infty}^{+\infty}\frac{e^{\mp k(z-z_c)}}{k}\frac{\sin\alpha x_c}{\alpha}\frac{\cos\beta y_c}{\beta}e^{j(\alpha x+\beta y)}d\alpha\, d\beta$$

$$z \gtrless z_c. \quad (17)$$

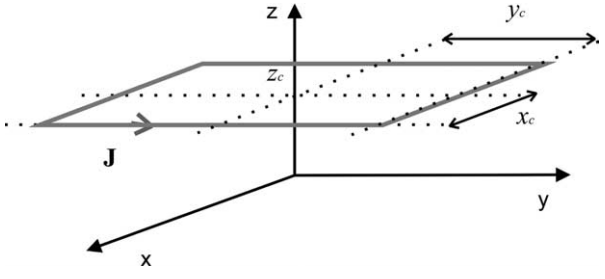

Fig. 2. Current carrying rectangular loop.

For the case of a loop centred at (x', y', z_c), the factor $e^{-j(\alpha x'+\beta y')}$ is introduced in the integrand of (17), as shown by an analogous calculation.

3.2. Rectangular spiral planar coils of finite rectangular cross-section

We want to calculate the EM fields of coils as those shown in Fig. 3, similar to those used in [7,8]. The usual technique for the construction of printed circuits was applied, i.e. the coils consist of rectangular spiral copper traces on a fiber glass substrate. The copper traces may lie on one or both faces of the substrate, and there may be more than one substrate per plate, the so called multi-layer design. A thin layer of epoxy resin protects the copper traces. Here, as in [7], single and two-layer coils have been used. In the present work, the following configurations are studied: a coil made of two rectangular 6-turn copper traces, each one deposited on the opposite faces of the isolating substrate (thus resulting in the upper and lower faces of a two layer coil), another similar coil but with two 10-turn copper traces and a third coil consisting of two parallel 7-turn copper traces on the same face of the substrate (single-layer coil). The width of the copper traces and the gap between them is 0.2 mm and their thickness is approximately 0.065 mm. All the coils are covered with a solder mask approximately 0.02 mm thick. In what follows these three coils will be referred to as coils 1, 2 and 3, respectively.

To deduce an expression for the fields and impedance of these coils, we calculate first the potential of a single rectangular loop of rectangular cross-section such as that shown in Fig. 4. For this calculation, we used the method presented in [10] for the calculation of the vector potential of a circular coil of finite rectangular cross-section, but applied to the deduction of the scalar potential W_{1ap}. The superposition principle is here applied to Eq. (17), assuming the excitation

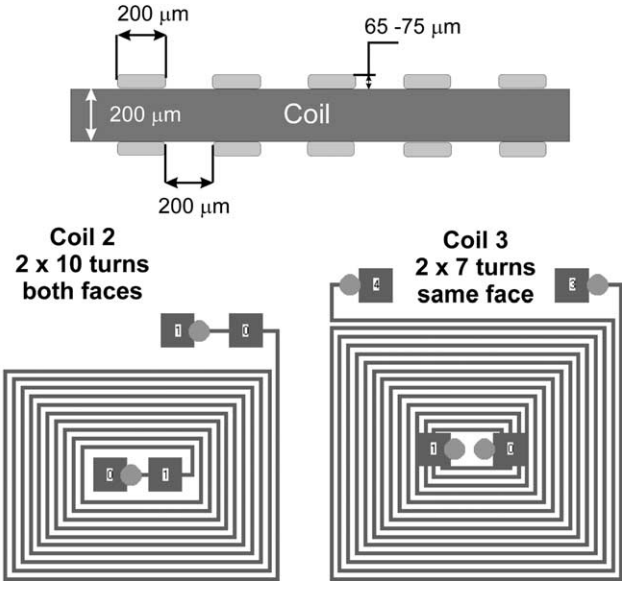

Fig. 3. General characteristics of the coils used and modelled. Side view of the upper and lower faces of a two-layer coil.

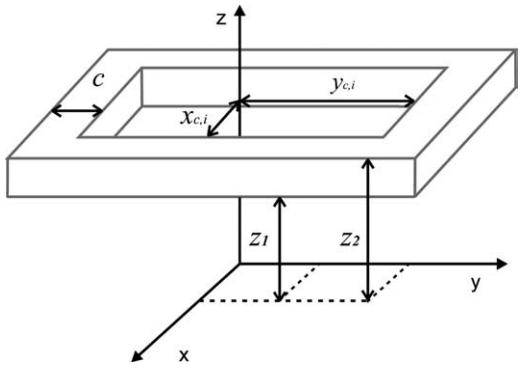

Fig. 4. Rectangular loop with a finite rectangular cross-section.

current density is constant in phase and amplitude over the loop cross-section. In particular in our coils, each turn in the spiral consisting of a single copper trace, the superposition is made by calculating the integral of W_{1ap}, Eq. (17), over the cross-section, but bearing in mind that this single copper trace is to be considered as a single 'turn of wire'. The expressions thus obtained for the scalar potential W_{1ap} of the loop in Fig. 4 in the different regions of space are presented in the Appendix A, and correspond to the expressions obtained in [9], but with number of turns $N=1$. As indicated in Fig. 4, in the formulae in the Appendix A and in what follows, z_1 and z_2 are the positions on the z-axis, such that z_2-z_1 is the thickness of the finite loop, the $(x_{c,i}, y_{c,i})$ pairs are the half-axes of the inner rectangle forming the loop (the sub indices i will be used in section when many turns are considered) and c is the width of the loop.

Once the expressions for the scalar potentials of a rectangular planar loop with a rectangular cross-section are known, the calculation of the scalar potentials for the coils under study is achieved by superposing concentric rectangular loops of the size corresponding to each turn of the spiral which makes each particular coil. In all these calculations, edge and skin effect, as well as the eddy currents inside the coils have been neglected. Moreover, the cross-section of each loop in the coil is assumed rectangular, though it is only approximately rectangular. A further approximation is that the spiral traces making the coils are substituted by the rectangular concentric loops.

The magnetic flux density in the no-conductor region R_a produced by the current circulating in the coils under study, is formed by the superposition of the fields produced by their $2n$ loops.

3.2.1. Coils 1 and 2

For coils 1 and 2, one half of the total $2n$ turns lie on one of the faces of the isolating substrate and the other half lie on the opposite face. One of these faces is denoted up, the fields produced by the loops on this face being indicated with the sub index u. Analogously, the opposite face is denoted down and the corresponding fields are indicated with the sub index d. Thus, the magnetic flux density in R_a we are calculating is

$$\mathbf{B}^{1ap}_{\text{Coils }1,2}=\sum_{i=1}^{n}(\mathbf{B}^{1ap}_{i,u}+\mathbf{B}^{1ap}_{i,d})=\nabla\frac{\partial}{\partial z}\sum_{i=1}^{n}(W_{1ap,i,u}+W_{1ap,i,d}). \tag{18}$$

For each $W_{1ap,i,u}$ and $W_{1ap,i,d}$ the expression (A2) from the Appendix A is used, the total scalar potential of the coils in free space thus being of the form

$$W^{TOT}_{1ap,\text{ Coils }1,2}=-\frac{\mu_0 I}{2\pi^2(z_2-z_1)c}\int_{-\infty}^{+\infty}\int_{-\infty}^{+\infty}\frac{e^{kz}}{k^2}\frac{\sum_{i=1}^{n}\Gamma(x_{c,i},y_{c,i})}{\alpha\beta}\times[e^{-kz_{2,u}}-e^{-kz_{1,u}}+e^{-kz_{2,d}}-e^{-kz_{1,d}}]e^{j(\alpha x+\beta y)}d\alpha\, d\beta \tag{19}$$

By comparison between (19) and (12) we deduce that the K^{TOT}_{1ap} coefficient, for a n-turn coil, is

$$K^{TOT}_{1ap,\text{Coils }1,2}=\frac{\mu_0 I}{2\pi^2(z_2-z_1)c}\frac{\sum_{i=1}^{n}\Gamma(x_{c,i},y_{c,i})}{\alpha\beta}\times\frac{[e^{-kz_{1,u}}-e^{-kz_{2,u}}+e^{-kz_{1,d}}-e^{-kz_{2,d}}]}{k^2}. \tag{20}$$

In (19) and (20): $z_{2,u}$, $z_{1,u}$, $z_{2,d}$ and $z_{1,d}$ are the z-axis positions of the upper and lower parts of the copper traces on the up and down faces of coils 1 and 2. Thus, $z_2-z_1=z_{2,u}-z_{1,u}=z_{2,d}-z_{1,d}$, is the thickness of the loops.

3.2.2. Coil 3

For coil 3, the $2n=14$ loops lie on the same face, in two parallel intertwined lanes having seven turns each. One of these lanes is called left and the fields produced by the loops in this lane are indicated with the sub index l. Analogously, the other lane is called right and the corresponding fields are indicated with the sub index r. The magnetic flux density in R_a produced by the coil is

$$\mathbf{B}^{1ap}_{\text{Coil }3}=\sum_{i=1}^{n}(\mathbf{B}^{1ap}_{i,l}+\mathbf{B}^{1ap}_{i,r})=\nabla\frac{\partial}{\partial z}\sum_{i=1}^{n}(W_{1ap,i,l}+W_{1ap,i,r}) \tag{21}$$

The loops which make the left spiral are centred at the point $(x', y')=(-0.2032\text{ mm}, -0.2032\text{ mm})$ on the plane of the coils, therefore in the expression for $W_{1ap,i,l}$ in (21), in which Eq. (A2) is used, the factor $e^{j(\alpha x'+y')}$, introduced in Section 3.1, is evaluated at that point. Similarly, the spiral denoted right is centred at the point $(x', y')=(0.2032\text{ mm}, 0.2032\text{ mm})$, the correction for $W_{1ap,i,r}$ being consequently evaluated at that point. Thus, the scalar potential for coil 3 is:

$$W^{TOT}_{1ap,\text{ Coil }3}=-\frac{\mu_0 I}{\pi^2(z_2-z_1)c}\int_{-\infty}^{+\infty}\int_{-\infty}^{+\infty}\frac{e^{kz}}{k^2}\frac{\sum_{i=1}^{n}\Gamma(x_{c,i},y_{c,i})}{\alpha\beta}\times[e^{-kz_2}-e^{-kz_1}]\cos[(\alpha+\beta)2.032\times10^{-4}]e^{j(\alpha x+\beta y)}d\alpha\, d\beta \tag{22}$$

From comparison between (22) and (12) the coefficient K_{1ap}^{TOT} for these type of coils is:

$$K_{1ap,\ Coil\ 3}^{TOT} = \frac{\mu_0 I}{\pi^2 (z_2 - z_1) c} \frac{\sum_{i=1}^{n} \Gamma(x_{c,i}, y_{c,i})}{\alpha\beta} \times \frac{[e^{-kz_1} - e^{-kz_2}]}{k^2} \cos[(\alpha + \beta) 2.032 \times 10^{-4}] \quad (23)$$

In (22) and (23) z_2 and z_1 are the z-coordinates of the upper and lower positions of the copper traces in coil 3.

With the formulae deduced in this section, together with (13) and (14), the scalar potentials of the coils under study can be calculated in all the regions of interest, and from them the EM fields are obtained.

4. Coil impedance

Coil impedance is calculated from the induced voltages on each of the loops making the coil, which are in turn calculated by superposition of the flux density produced by each particular loop through itself and through all the others.

Let us first consider any single loop i in the coil. Let $\mathbf{B}_i^{TOT}$ be the sum of the magnetic flux densities through the area bounded by loop i produced by loop i itself, all the other loops in the coil and the induced currents in the material. Then the induced voltage on loop i is

$$V_i^{TOT} = \frac{j\omega}{(z_2 - z_1) c} \int_{\text{Coil crosssection}} \left(\int_{S_i} \hat{\mathbf{z}} \mathbf{B}_i^{TOT} da_i \right) \text{d Area}_i \quad (24)$$

On the other hand, we know that:

$$V = IZ = I(Z_0 + \Delta Z), \quad (25)$$

$$Z_0 = jX_0 = j\omega L_0 \quad (26)$$

and

$$\Delta Z = \Delta R + j\Delta X. \quad (27)$$

Here, Z_0 is the coil impedance in air and ΔZ is the impedance change produced by the currents induced in the conducting material.

4.1. L_0 coil inductance

In this case, the $\mathbf{B}_i^{TOT}$ field in (24) is the flux density through loop i produced by the coil in free space. As explained above, the active fields in each particular loop i in the coil are its own, namely $\mathbf{B}_i^{1ap}$, and that produced by the other loops in the entire coil.

4.1.1. Coils 1 and 2

Let loop i lie on the up face and $\mathbf{B}_{1ap,iu}^{TOT}$ be the total flux density through that loop. Then the z component in (24) is

$$B_{z,1ap,i,u}^{TOT} = \sum_{nu=1}^{n} B_{z,iu,nu}^{1ap} + \sum_{nd=1}^{n} B_{z,iu,nd}^{1ap}. \quad (28)$$

Each of the $B_{z,iu,nu}^{1ap}$ is given by (A3) through (7), and each of the $B_{z,iu,nd}^{1ap}$ is given by (A1), also through (7). The reader is referred to the Appendix A for both cases. Using (22) and (28), the total induced voltage on loop iu is

$$\begin{aligned} V_{1ap,iu}^{TOT} = & \frac{2j\omega I\mu_0}{\pi^2 (z_2 - z_1)^2 c^2} \\ & \times \left\{ \int_{-\infty}^{+\infty} \int_{-\infty}^{+\infty} 2 \left[(z_{2,u} - z_{1,u}) + \frac{(e^{-k(z_{2,u} - z_{1,u})} - 1)}{k} \right] \right. \\ & \times \frac{\sum_{nu=1}^{n} \Gamma(x_{c,nu}, y_{c,nu})}{(\alpha\beta)^2} \Gamma(x_{c,iu}, y_{c,iu}) d\alpha\, d\beta \\ & + \int_{-\infty}^{+\infty} \int_{-\infty}^{+\infty} \left[\frac{(e^{-kz_{1,u}} - e^{-kz_{2,u}})(e^{kz_{2,d}} - e^{kz_{1,u}})}{k} \right] \\ & \left. \times \frac{\sum_{nd=1}^{n} \Gamma(x_{c,nd}, y_{c,nd})}{(\alpha\beta)^2} \Gamma(x_{c,iu}, y_{c,iu}) d\alpha\, d\beta \right\} \end{aligned} \quad (29)$$

The total induced voltage on all the coil deposited on face u is the sum of the voltages $V_{1ap,iu}^{TOT}$ on each loop iu of that face. Let $V_{1ap,u}^{TOT}$ be that voltage

$$\begin{aligned} V_{1ap,u}^{TOT} = & \frac{16j\omega I\mu_0}{\pi^2 (z_2 - z_1)^2 c^2} \left\{ \int_{0}^{+\infty} \int_{0}^{+\infty} \left[(z_{2,u} - z_{1,u}) \right. \right. \\ & \left. + \frac{(e^{-k(z_{2,u} - z_{1,u})} - 1)}{k} \right] \frac{\left[\sum_{n=1}^{n} \Gamma(x_{c,n}, y_{c,n}) \right]^2}{(\alpha\beta)^2} d\alpha\, d\beta \\ & + \int_{0}^{+\infty} \int_{0}^{+\infty} \left[\frac{(e^{-kz_{1,u}} - e^{-kz_{2,u}})(e^{-kz_{2,d}} - e^{-kz_{1,d}})}{2k} \right] \\ & \left. \times \frac{\left[\sum_{n=1}^{n} \Gamma(x_{c,n}, y_{c,n}) \right]^2}{(\alpha\beta)^2} d\alpha\, d\beta \right\} \end{aligned} \quad (30)$$

Besides, $V_{1ap,u}^{TOT} = j\omega I L_{0,u}$ and, because of coil symmetry the inductance in air results

$$L_{0,\ Coils\ 1,2} = 2L_{0,u}. \quad (31)$$

4.1.2. Coil 3

Loop i of coil 3 lies on the same face of the isolating substrate as all the other loops making the coil. Let that coil belong to the left spiral and $\mathbf{B}_{1ap,il}^{TOT}$ be the total flux density through that loop, then the z component is:

$$B_{z,1ap,il}^{TOT} = \sum_{nl=1}^{n} B_{z,il,nl}^{1ap} + \sum_{nr=1}^{n} B_{z,il,nr}^{1ap}. \quad (32)$$

Here, both $B^{1ap}_{z,il,nl}$ and $B^{1ap}_{z,il,nr}$ are calculated applying (7) and (A3) to these coils; but with the corrections due to the position of the centre of spirals l and r, that is, the factor $e^{-j(\alpha x' + \beta y')}$ must be evaluated as indicated in Section 3.2.1. From (24), but now with (32), the induced voltage on loop il is

$$V^{TOT}_{1ap,il} = \frac{8j\omega I\mu_0}{\pi^2(z_2-z_1)^2c^2}\int_{-\infty}^{+\infty}\int_{-\infty}^{+\infty}\left[(z_2-z_1)+\frac{\left(e^{-k(z_2-z_1)}-1\right)}{k}\right] \times \frac{\sum_{m=1}^{n}\Gamma(x_{c,m},y_{c,m})}{(\alpha\beta)^2}\Gamma(x_{c,il}y_{c,il}) \times \cos[2.032\times10^{-4}(\alpha+\beta)]\mathrm{d}\alpha\,\mathrm{d}\beta. \quad (33)$$

The total induced voltage on all the l coil is the sum of the voltages $V^{TOT}_{1ap,i,l}$ on all of its il loops. Let $V^{TOT}_{1ap,l}$ be that voltage. Then

$$V^{TOT}_{1ap,l} = \frac{8j\omega I\mu_0}{\pi^2(z_2-z_1)^2c^2}\int_{-\infty}^{+\infty}\int_{-\infty}^{+\infty}\left[(z_2-z_1)+\frac{\left(e^{-k(z_2-z_1)}-1\right)}{k}\right] \times \frac{\left[\sum_{m=1}^{n}\Gamma(x_{c,m},y_{c,m})\right]^2}{(\alpha\beta)^2}\cos[2.032\times10^{-4}(\alpha+\beta)]\mathrm{d}\alpha\,\mathrm{d}\beta \quad (34)$$

In (32)–(34), sub index m stands for m = nl = nr.

Besides, $V^{TOT}_{1ap,l} = j\omega I L_{0,l}$, and

$$L_{0,\ \mathrm{Coil}\ 3} = 2L_{0,l}. \quad (35)$$

4.2. Coil ΔZ

For the calculation of the impedance change produced by the currents induced in the conducting material, the expression derived by Auld et al. in [18] was used:

$$\Delta Z = \frac{1}{I^2}\oint_{S_c}\hat{\mathbf{n}}\cdot(\mathbf{E}^0\times\mathbf{H}^c-\mathbf{E}^c\times\mathbf{H}^0)\mathrm{d}S_c. \quad (36)$$

Here, S_c is an arbitrary closed surface enclosing the conductor but excluding the coil. $\mathbf{E}^0$ and $\mathbf{H}^0$ are the fields in absence of the conductor, while $\mathbf{E}^c$ and $\mathbf{H}^c$ are the fields in its presence. The surface S_c is that of the conductor (at $z=0$) and is closed at infinity by surface S_∞ which extends within the conductor for $z<0$. With this choice for S_c, applying (7) and vector identities to the integrand in (36), and considering the divergence theorem and Farady's law, Eq. (36) becomes

$$\Delta Z = -\frac{j\omega}{\mu_0 I^2} \times \int_{-\infty}^{+\infty}\int_{-\infty}^{-\infty}\left(\frac{\partial^2 W_0}{\partial z^2}\frac{\partial W_c}{\partial z}-\frac{\partial^2 W_c}{\partial z^2}\frac{\partial W_0}{\partial z}\right)_{(z=0)}\mathrm{d}x\,\mathrm{d}y \quad (37)$$

For our problem, $W_0 = W_{1ap}$ and $W_c = W_{1ap} + W_{1as}$. From the calculation of each of the factors in the integrand of (37) using (12) and (13) the expression for ΔZ results:

$$\Delta Z = \frac{j8\pi^2\omega}{\mu_0 I^2}\int_{-\infty}^{+\infty}\int_{-\infty}^{-\infty}k^3 K_{1ap}(\alpha,\beta)K_{1ap}(-\alpha,-\beta) \times \frac{\mu_r k-\gamma}{\mu_r k+\gamma}\mathrm{d}\alpha\,\mathrm{d}\beta \quad (38)$$

This is a general expression, valid for any particular distribution determined by K_{1ap}.

4.2.1. Coils 1 and 2

For coils 1 and 2, the K_{1ap} factor in the integrand of (38) is given by (20). Considering that $K^{TOT}_{1ap,\ \mathrm{Coils}\ 1,2}(\alpha,\beta) = K^{TOT}_{1ap,\ \mathrm{Coils}\ 1,2}(-\alpha,-\beta)$ and substituting (20) in (38) we get the expression for the impedance change due to the presence of the conducting material

$$\Delta Z_{\mathrm{Coils}\ 1,2} = \frac{j8\omega\mu_0}{\pi^2(z_2-z_1)^2c^2}\int_0^{+\infty}\int_0^{-\infty}\frac{\left[\sum_{i=1}^{n}\Gamma(x_{c,i},y_{c,i})\right]^2}{(\alpha\beta)^2} \times \frac{[e^{-kz_{1,u}}-e^{-kz_{2,u}}+e^{-kz_{1,d}}-e^{-kz_{2,d}}]^2}{k} \times \frac{\mu_r k-\gamma}{\mu_r k+\gamma}\mathrm{d}\alpha\,\mathrm{d}\beta \quad (39)$$

4.2.2. Coil 3

The factor K_{1ap} for coil 3 is given by (23). Here also $K^{TOT}_{1ap,\ \mathrm{Coil}\ 3}(\alpha,\beta) = K^{TOT}_{1ap,\ \mathrm{Coils}\ 3}(-\alpha,-\beta)$, thus analogously to the procedure for coils 1 and 2, the impedance change of coil 3 due to the presence of the conducting material is

$$\Delta Z_{\mathrm{Coils}\ 3} = \frac{j32\omega\mu_0}{\pi^2(z_2-z_1)^2c^2}\int_0^{+\infty}\int_0^{-\infty}\frac{\left[\sum_{i=1}^{n}\Gamma(x_{c,i},y_{c,i})\right]^2}{(\alpha\beta)^2} \times \frac{[e^{-kz_1}-e^{-kz_2}]^2}{k}\frac{\mu_r k-\gamma}{\mu_r k+\gamma}\cos^2[2.032 \times 10^{-4}(\alpha+\beta)]\mathrm{d}\alpha\,\mathrm{d}\beta. \quad (40)$$

5. Implementation and results

In order to determine the scope and validity of the derived formulae, we calculated first the values of L_0, the inductance in air of the coils under study, and compared them with the measured values. Eqs. (30) and (31) were used for coils 1 and 2 and Eqs. (34) and (35) for coil 3. The measurements for coils 2 and 3 were presented in [7]. They were made using a resonant R–L–C circuit, as explained there. These results as well as the measurements corresponding to

Table 1
Calculated and measured in-air inductances of the three coils under study

	$L_{0,\text{Calculated}}$ (μHy)	$L_{0,\text{Measured}}$ (μHy)	Δ%
Coil 1	0.98	1.23±0.03	20.3
Coil 2	3.20	3.38±0.03	5.3
Coil 3	1.45	1.58±0.02	8.2

coil 1 are presented in Table 1. Column 4 of Table 1 shows the percentage difference (Δ%) of the calculated L_0 with respect to the experimental L_0. Considering the approximations in these calculations, it may be said that the theoretical derivations presented here yield predictions of L_0.

As mentioned above, the L_0 measured values for the three coils, which are compared with the calculated values, were obtained using a R–L–C resonant circuit. The resonance frequency, f_r, is measured in this circuit; and then L_0 is obtained through the expression: $L_0(f_r, C)=1/(2\pi f_r)^2 C$. The value of C that appears in this formula is known and is determined with its correspondent error, just like f_r. The error in L_0 is then calculated by error propagation for the expression above. The values shown in the third column of Table 1 were calculated in that way. Of the two magnitudes in the formula, the capacity and the frequency of resonance, the latter and its error are the magnitudes, which have the most influence in the calculation of L_0 and its error.

In addition to the quasi-stationary approximation introduced in Section 2, the following approximations, mentioned in Section 3.2, were considered for the application of the model developed to the coils in question:

- In all these calculations, edge and skin effect, as well as the eddy currents inside the coils have been neglected.
- Moreover, the cross-section of each loop in the coil is assumed rectangular, though it is only approximately rectangular.
- A further approximation is that the spiral traces making the coils are substituted by the rectangular concentric loops.

These last two approximations are the ones that have the most severe influence in the theoretical description of the real coils, possibly because this kind of approximations are directly related to the actual shape of the coils. As to the approximation of the spirals by concentric rectangular loops, it is no surprise that it will be a better description of the real coils if the spiral tracks are very narrow and very close to each other. The fact that assuming a rectangular cross-section is an approximation can be evaluated by optical microscopy of a cut of the copper traces of the coils, see Fig. 5. As it can be seen in this figure, there is a rectangular section plus a trapezoidal one. The area taken for the calculation was a rectangular equivalent section of the same area as the sum of the rectangle plus the trapezoid areas. This approximation will be a better description of the real coils as the cross-section of the copper tracks decreases.

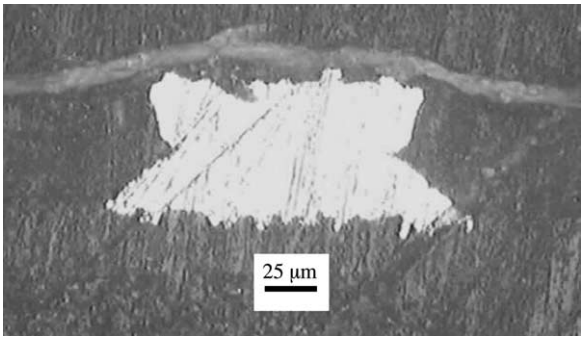

Fig. 5. Cross-section of a cooper trace.

There is an aspect of the real coils, which has not been taken into account in the calculation and also explains in part the discrepancy among the calculated and measured values of L_0, specially for coil 1 which showed the bigger discrepancy (see Table 1). This aspect is related to the manufacture of the coils, and it is that in the central part of the coils we have constructed the connectors, on which the cables are to be welded (see Fig. 3). These connectors are also made of copper as the spiral tracks; but they are quite larger: they are 1.6 mm side squares. The variation of the electromagnetic field in the surface of these square connectors produces an increment in the impedance of the coils. This variation would explain, in part, that with our calculations we always obtain values smaller than the measured ones. Thus, this increment in the inductance relative to the total area of the coil is more important for the smaller coil than for the bigger ones. This would explain the bigger discrepancy between the calculated and the measured value of L_0 for the coil 1.

With the expressions (39) and (40) together with (25), the impedance diagrams for the inductors under study were determined in different conditions. For the simulations, lift-off values between 0 and 30 mm and excitation frequencies between 0 and 100 MHz were considered. All the frequency range for eddy current testing was thus covered. As the materials for the conducting half-spaces, Zircaloy-4 (Zry-4) and aluminum were selected. Their electrical conductivities are 1.35×10^6 S/m [19] and 3.56×10^7 S/m [20], respectively, and both have $\mu_r=1$. Impedance diagrams were also calculated varying the conductivity of the half-space in all the possible range, to obtain a full diagram. As is usual practice in eddy current testing, the complex impedance given by (25) is normalized to X_0, the inductive reactance of the coil in air.

Fig. 6 shows the impedance diagrams for Zry-4 and Al of the three coils under study, when frequency is varied. A 2.0×10^{-5} m lift-off was used for the calculation, that being the approximate thickness of the solder mask. At first glance, it may be stated that the characteristics of the diagrams depend on the type of coil (i.e. basically its geometry), independent of the material of the conducting half-space.

As it can be observed, $\Delta Z_{\text{Coil 3}} \ll \Delta Z_{\text{Coils 1,2}}$ and $\Delta Z_{\text{Coil1}} \cong \Delta Z_{\text{Coil2}}$ for all the frequencies. We conclude that at all frequencies the coupling between coil 3 and the conducting material is weaker than that of the two others. We postulate this is basically due to the respective single-layer, two-layer design of the coils and not to the number of turns itself. The lift-off traces produced by coil 3 in Fig. 6 are thus smaller than those of the other two. Though this fact might seem beneficial at

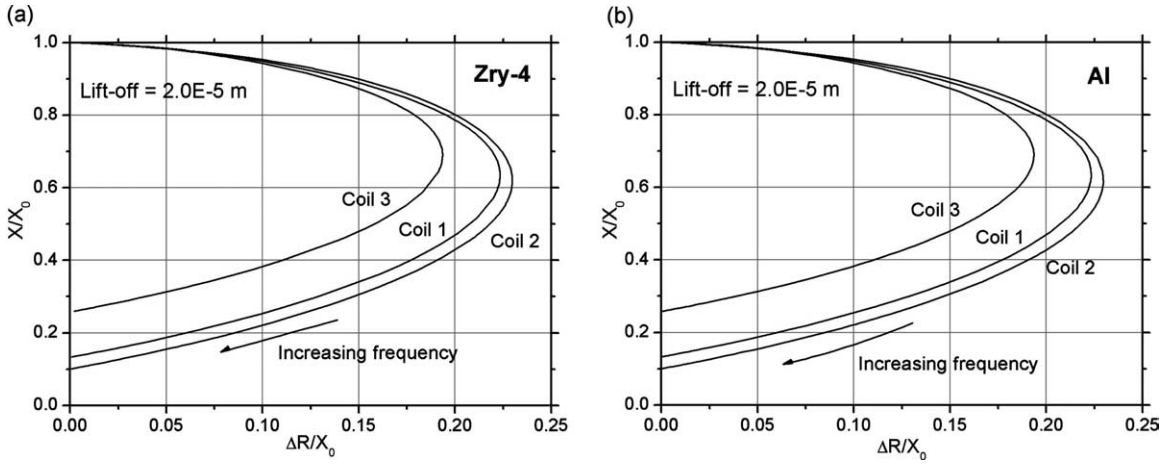

Fig. 6. Impedance diagrams made varying the excitation frequency.

inspection time, it is actually not so, because the signals from this coil need greater amplification, thus amplifying also unwanted noises and lowering signal to noise ratio.

Impedance diagrams were also calculated for the full frequency range and different lift-off values. Fig. 7 shows one of these diagrams. From these calculations, the limiting lift-off value, for which the lack of coupling between material and coil starts being significant, can be estimated. It must be pointed out that the above-mentioned 2.0×10^{-5} m lift-off curve is not shown in Fig. 7 because it differed non-significantly from the zero lift-off curve (compare Fig. 6).

The optimal frequency for conductivity measurement was determined in an approximate way for each coil and each conducting material. Following [21], this frequency is that for which $\Delta R/X_0$ is maximum in an impedance diagram such as those in Fig. 6. Graphically it corresponds to the extreme right portion of the nose-shaped diagrams. These optimal frequencies are listed in Table 2.

In order to compare our sensors' response to conductivity changes, some conductivity variation assessment tests have been modelled for Zry-4 and Al. The calculations were made at the optimal frequencies and at frequencies quite higher than those. The higher frequencies were prompted by the experience in the use of these sensors. In the experiments reported in [7,8], and in other experiments performed with these sensors in the group, good response for material sorting was observed at frequencies quite higher than the theoretical optimal frequencies determined here. As an example, for Zry-4, hydrided Zry-4 and low conductivity materials, the best responses were those at frequencies above 300 kHz, even as high as 1 MHz. Therefore, calculations for Zry-4 were also made at 800 kHz as the alternative frequency. The alternative frequency for Al was selected such that it produced in Al the same standard skin-depth as 800 kHz in Zry-4. The alternative frequency for Al thus determined is approximately 30 kHz. The results are shown in Figs. 8 and 9.

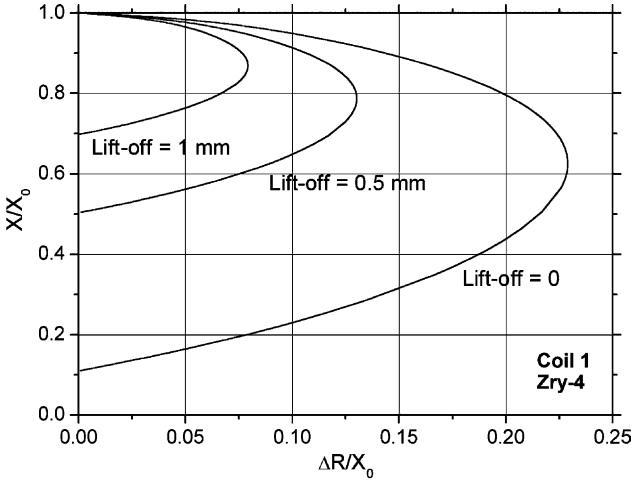

Fig. 7. Impedance diagrams made varying the excitation frequency, for three lift-off values.

The shape of these curves is that of the well-known lift-off signals. Just to explain the origin and shape of these signals, it must be pointed out that in these kind of eddy-current experiments, the Wheatstone bridge constituting the normal equipment—to one branch of which the sensor is connected—is balanced while the sensor is 'in air' (i.e. far from the conducting material). The experiment consists on recording the bridge 'unbalance' while the sensor is approached to the material [21]. For the present calculations, lift-off was varied between 30 and 0 mm. The simulations were made using the conductivities of Zry-4 and Al, full-line curves in Figs. 8 and 9, and then $\pm15\%$ variations to those conductivities were considered (dotted-line curves). These variations were arbitrarily chosen. For

Table 2
Optimal frequencies for conductivity assessment

Optimal frequencies (kHz)	Coil 1	Coil 2	Coil 3
Zry-4	150	75	145
Al	5.5	3	5.5

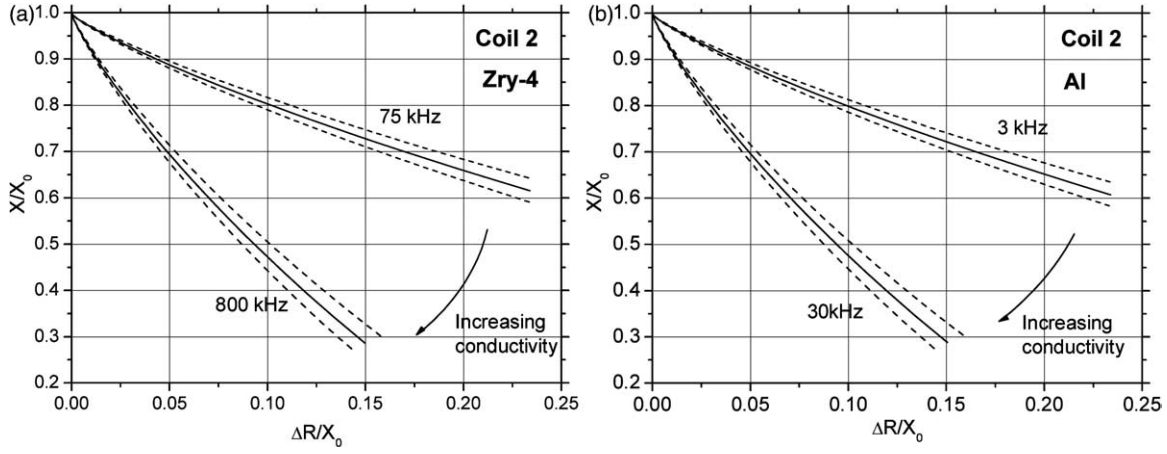

Fig. 8. Simulated conductivity assessment tests with coil 2.

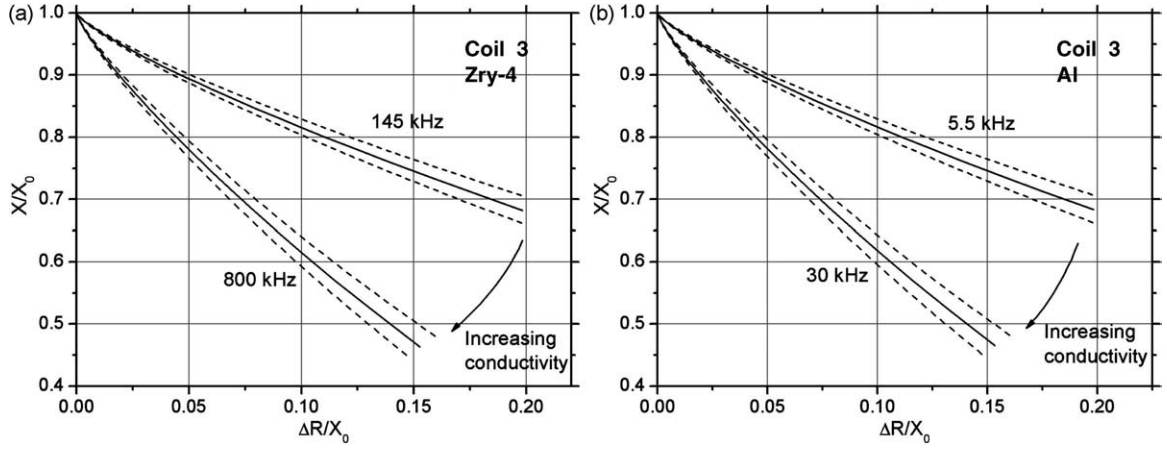

Fig. 9. Simulated conductivity assessment tests with coil 3.

each of the coils it can be generally stated that for both materials the sorting power of the coils is similar at the frequencies defined as optimal in the handbooks and at the higher frequencies. Another aspect, which results from the comparison between Figs. 8 and 9 is that because the full lift-off signal from coil 3 is quite smaller than those from coils 1 and 2, the relative variations between the different signals are smaller for coil 3 than for the two others. For instance, at the optimal frequencies in the conductivity range studied (-15 to $+15\%$), the variations for coil 2 lie in an interval of approximately 0.05 units on the X/X_0 axis (similar values being determined for coil 1), while the variations for coil 3 lie in an interval of approximately 0.04 units on the same axis. This is another consequence of the lower coupling with the material to be inspected which coil 3 presents as compared to the other two coils.

Finally, impedance diagrams for conductivity variation were calculated. This was made for the three coils at the optimal frequencies defined here and zero lift-off. The results for $f=3$ kHz are shown in Fig. 10. Here, as for the analysis of Fig. 6, it can be stated that diagram characteristics depend on coil design and not on the conductivity of the material to be inspected. In the analysis of Fig. 10 this last point is more evident, because the diagrams here are produced when conductivity varies throughout the complete range for metals.

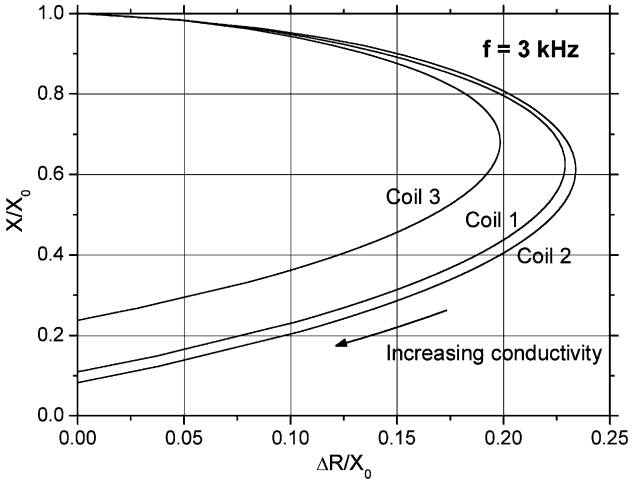

Fig. 10. Impedance diagrams made varying the conductivity.

6. Conclusions

Analytical expressions for the EM fields produced by rectangular planar spiral coils with finite cross-section were obtained with the second order vector potential method. The knowledge of these fields enabled us to calculate the electrical parameters of the coils and model their impedance diagrams.

The comparison of the calculated self-inductance in air of the coils under study and the measurements on real coils showed that the theoretical derivations presented here are acceptable for determining that parameter.

The construction of the impedance diagrams led us to conclude that coil design is determinant as to the coupling between the coil and the conducting material, independent of material properties. Thus, the coupling of the coil having two planar windings on the same face of the isolating substrate (coil 3) is remarkably lower than that of the coils having their planar windings on opposite faces of the substrate. The consequences of the lower coupling properties of coil 3 as compared with the two others were observed in the experimental work, both in conductivity assessment and crack detection on flat components [7,8].

The determination of the impedance diagrams enabled us to estimate also at which lift-off value, lack of coupling between material and sensor acquires importance in a given work condition.

With the full impedance diagrams constructed varying the frequency in all the usual range for eddy current testing, the optimal frequency for conductivity assessment could be evaluated for each coil and material (according to handbooks [21]). Simulated conductivity experiments at the optimal frequencies and at another set of frequencies (quite higher than the optimal frequencies and empirically established at our laboratory) showed that the resolving power of these sensors for material sorting is similar at both frequency groups.

The establishment of analytical expressions for the EM fields of this type of coils with an acceptable approximation will be particularly helpful and useful to us, especially for the design of new coils and /or for the prediction of the performance of the coils we have under new test conditions.

Acknowledgements

The authors thank Dr Theodoros Theodoulidis, from the University of West Macedonia, Greece, for his most valuable private communications with one of us (JOF). They thank J. Marengo from the Special Techniques Laboratory and A. Acosta from the Precision Workshop for their cooperation with the experimental work. They are also grateful to CNEA and CONICET and acknowledge funding from the Argentine R/D Agency, ANPCYT's through research projects PICT 12113 and 14426.

Appendix A

The application of the superposition principle with (17) to a configuration like that in Fig. 4 (i.e. a single rectangular loop of finite cross-section) which leads to the expressions for the scalar fields, is presented [9] with the following results:

$$W_{1ap} = \frac{\mu_0 NI}{2\pi^2(z_2 - z_1)c} \int_{-\infty}^{+\infty}\int_{-\infty}^{+\infty} \frac{\Gamma(x_{c,i},y_{c,i})}{\alpha\beta} \frac{e^{-kz}}{k^2} [e^{kz_2} - e^{kz_1}] e^{j(\alpha x+\beta y)} d\alpha\, d\beta \quad \text{(A1)}$$

for $z > z_2$,

$$W_{1ap} = -\frac{\mu_0 NI}{2\pi^2(z_2 - z_1)c} \int_{-\infty}^{+\infty}\int_{-\infty}^{+\infty} \frac{\Gamma(x_{c,i},y_{c,i})}{\alpha\beta} \frac{e^{kz}}{k^2} [e^{-kz_2} - e^{-kz_1}] e^{j(\alpha x+\beta y)} d\alpha\, d\beta \quad \text{(A2)}$$

for $z < z_1$ and

$$W_{1ap} = \frac{\mu_0 NI}{2\pi^2(z_2 - z_1)c} \int_{-\infty}^{+\infty}\int_{-\infty}^{+\infty} \frac{\Gamma(x_{c,i},y_{c,i})}{\alpha\beta} \times \frac{[2 - e^{-k(z-z_1)} - e^{k(z-z_2)}]}{k^2} e^{j(\alpha x+\beta y)} d\alpha\, d\beta \quad \text{(A3)}$$

for $z_1 \le z \le z_2$.

As mentioned in Section 4.2, in the case of our loops, the number of wire turns $N = 1$.

The function $\Gamma(x_{ci}, y_{ci})$ contains the geometry and dimensions of the coil [9]

$$\Gamma(x_{ci},y_{ci}) = \int_0^c \sin\alpha(x_{ci}+c)\sin\beta(y_{ci}+c)dc$$

$$= \begin{cases} \dfrac{\sin[(\alpha-\beta)c + \alpha x_{ci} - \beta y_{ci}] - \sin(\alpha x_{ci} - \beta y_{ci})}{2(\alpha-\beta)} - \dfrac{\sin[(\alpha+\beta)c + \alpha x_{ci} + \beta y_{ci}] - \sin(\alpha x_{ci} + \beta y_{ci})}{2(\alpha+\beta)} & \text{si } \alpha \neq \beta \\ \dfrac{c}{2}\cos[\alpha(x_{ci}-y_{ci})] - \dfrac{\sin[\alpha(2c + x_{ci} + y_{ci})]}{4\alpha} - \dfrac{\sin[\alpha(x_{ci}+y_{ci})]}{4\alpha} & \text{si } \alpha = \beta \end{cases}$$

References

[1] Yamada S, Katoun M, Iwahara M, Dawson FP. Eddy current testing probe composed of planar coils. IEEE Trans Magn 1995;31(6):3185–7.

[2] Yamada S, Katoun M, Iwahara M, Dawson FP. Defect images by planar ECT probe of meander-mesh coils. IEEE Trans Magn 1996;32(5): 4956–8.
[3] Yamada S, Fujiki H, Iwahara M, Mukhopadhyay SC, Dawson FP. Investigation of printed wiring board testing by planar coil type ECT probe. IEEE Trans Magn 1997;33(5):3376–8.
[4] Kawabe K, Koyama H, Shirae K. Planar inductor. IEEE Trans Magn 1984;MAG-20(5):1804–6.
[5] Ebine N, Ara K. Magnetic measurement to evaluate material properties of ferromagnetic structural steels with planar coils. IEEE Trans Magn 1999; 35(5):3928–30.
[6] Pedersen LB, KÅ Magnusson, Zhengsheng Y. Eddy current testing of thin layers using co-planar coils. Res Nondestruct Eval 2000;12(1): 53–64.
[7] Fava J, Ruch M. Design, construction and characterization of ECT sensors with rectangular planar coils. Insight 2004;46(5):268–74.
[8] Fava J. Diseño y construcción de sondas para ensayos por corrientes inducidas conteniendo bobinas planas rectangulares. Tesis para optar al título de Magíster en Ciencia y Tecnología de Materiales; 2003.
[9] Theodoulidis TP, Kriezis EE. Impedance evaluation of rectangular coils for eddy current testing of planar media. NDT&E Int 2002;35:407–14.
[10] Dodd CV, Deeds WE. Analytical solution to eddy-current probe-coil problems. J Appl Phys 1968;39(6):2829–38.
[11] Smythe WR. Static and dynamic electricity. 3rd ed. New York: MacGraw-Hill; 1968. p. 284–6.
[12] Jackson JD. Classical electrodynamics. 2nd ed. New York: Wiley; 1974. p. 219–23.
[13] Libby HL. Introduction to electromagnetic nondestructive test methods. New York: Wiley; 1971. p. 145.
[14] Kriezis EE, Xypteras IE. Eddy current distribution and loss in a semi-infinite conducting space due to vertical current loop. ETZ Arch 1979;7: 201–7.
[15] Bowler JR. Eddy current calculations using half-space green's functions. J Appl Phys 1987;61(3):833–9.
[16] Hsu HP. Análisis de Fourier. Bogotá: Addison-Wesley Iberoamericana; 1987.
[17] Feynman RP, Leighton RB, Sands M. The feynman lectures on physics. New York: Addison-Wesley; 1966 [chapter 14].
[18] Auld BA, Muennemann FG, Riaziat M. Quantitative modelling of flaw response in eddy current testing. In: Sharpe RS, editor. Research techniques in nondestructive testing. New York: Academic Press; 1984. p. 37–76.
[19] ASM metals handbook 10th ed, vol. 2. Ohio; 1990.
[20] ASM metals handbook 9th ed, vol. 2. Ohio; 1979.
[21] Cecco SS, Van Drunen G, Sharp FL. Eddy current manual, vol. 1. Ontario: Chalk River Nuclear Laboratories, Atomic Energy of Canada Limited; 1981 p. 80–2.